

# Shape transitions in exotic Si and S isotopes and tensor-force-driven Jahn-Teller effect

Yutaka Utsuno,<sup>1,2</sup> Takaharu Otsuka,<sup>3,2,4</sup> B. Alex Brown,<sup>4,5</sup>  
Michio Honma,<sup>6</sup> Takahiro Mizusaki,<sup>7</sup> and Noritaka Shimizu<sup>2</sup>

<sup>1</sup>Advanced Science Research Center, Japan Atomic Energy Agency, Tokai, Ibaraki 319-1195, Japan

<sup>2</sup>Center for Nuclear Study, University of Tokyo, Hongo, Bunkyo-ku, Tokyo 113-0033, Japan

<sup>3</sup>Department of Physics, University of Tokyo, Hongo, Bunkyo-ku, Tokyo 113-0033, Japan

<sup>4</sup>National Superconducting Cyclotron Laboratory, Michigan State University, East Lansing MI 48824, USA

<sup>5</sup>Department of Physics, Michigan State University, East Lansing MI 48824, USA

<sup>6</sup>Center for Mathematical Sciences, University of Aizu,

Ikki-machi, Aizu-Wakamatsu, Fukushima 965-8580, Japan

<sup>7</sup>Institute for Natural Sciences, Senshu University, Tokyo, 101-8425, Japan

(Dated: October 16, 2018)

We show how shape transitions in the neutron-rich exotic Si and S isotopes occur in terms of shell-model calculations with a newly constructed Hamiltonian based on  $V_{\text{MU}}$  interaction. We first compare the calculated spectroscopic-strength distributions for the proton  $0d_{5/2,3/2}$  and  $1s_{1/2}$  orbitals with results extracted from a  $^{48}\text{Ca}(e,e'p)$  experiment to show the importance of the tensor-force component of the Hamiltonian. Detailed calculations for the excitation energies,  $B(E2)$  and two-neutron separation energies for the Si and S isotopes show excellent agreement with experimental data. The potential energy surface exhibits rapid shape transitions along the isotopic chains towards  $N=28$  that are different for Si and S. We explain the results in terms of an intuitive picture involving a Jahn-Teller-type effect that is sensitive to the tensor-force-driven shell evolution. The closed sub-shell nucleus  $^{42}\text{Si}$  is a particularly good example of how the tensor-force-driven Jahn-Teller mechanism leads to a strong oblate rather than spherical shape.

PACS numbers: 21.60.Cs.,27.40.+z,21.10.Pc,21.10.-k,21.30.Fe

Among the new frontiers of nuclear physics, one of the most important is the evolution of single-particle energies in nuclei far from stability that led to significant variation of the shell structure and even dramatic changes in the location of magic numbers [1, 2]. One of the ingredients is the tensor force which can change spin-orbit splitting significantly leading to tensor-force driven shell evolution [3, 4]. While many experimental examples, *e.g.*, [5–8], have been accumulated on this phenomenon, its direct test including fragmentation of single-particle strength has not been presented. We shall show, in this paper, the first test of this kind for proton  $0d_{5/2}$ - $0d_{3/2}$  splitting in  $^{48}\text{Ca}$ , comparing to spectroscopic factors measured in the  $(e,e'p)$  experiment [9].

We shall then show<sup>1</sup> that tensor-driven shell evolution plays a critical role in the rapid shape transition as a function of neutron and/or proton number, including tri-axial and  $\gamma$ -unstable shapes. In particular, we show for the first time how this shape transition at low energy can be related to the Jahn-Teller type effect [11, 12], where a geometric distortion is brought about by a particular coherent superposition of relevant single-particle states enhanced due to their (near) degeneracy.

These studies are performed in terms of the shell model in a unified way with a new Hamiltonian. We shall show

calculated energy levels and  $B(E2)$  values for the Si and S isotopes that are in good agreement with experiments [13–19], and new predictions are made. Potential energy surfaces (PES) are shown. The PES changes rapidly as a function of neutron number, and are different for Si and S. The PES for  $^{42}\text{Si}$  shows a strong oblate shape (rather than spherical) due to the tensor-force-driven shell evolution. These PES results are interpreted in an intuitive picture involving shell gaps and the Jahn-Teller-type effect. Two-neutron separation energies are discussed also.

We outline the present shell-model calculations. The  $sd$  and  $pf$  shells are taken as the valence shell with protons in  $sd$  and neutrons in  $pf$ . The interactions within each of these shells are based on existing interactions: USD [20] (GXPF1B [21]<sup>2</sup>) for the  $sd$  ( $pf$ ) shell, except for the monopole interactions [4, 23]  $V_{0d_{3/2},0d_{5/2}}^{T=0,1}$  based on SDPF-M [24] due to a problem in USD as pointed out in [2]. The monopole- and quadrupole-pairing matrix elements  $\langle 0f_{7/2}0f_{7/2} | V | 0f_{7/2}0f_{7/2} \rangle_{J=0,2}$  are replaced with those of KB3 [23]. This is mainly for a better description of nuclei of  $N \sim 22$ . Although this replacement is not so relevant to the present study where  $N$  is larger in most cases, it has been made so that the applicabil-

<sup>1</sup> A brief account with selected results of this work was presented in [10].

<sup>2</sup> GXPF1B Hamiltonian was created from GXPF1A Hamiltonian [22] by changing five  $T = 1$  matrix elements and SPE involving  $1p_{1/2}$ . Such differences give no notable change to the present work due to minor relevance of  $1p_{1/2}$ .

ity of the new Hamiltonian becomes wider. The cross-shell part, most essential for exotic nuclei discussed in this study but rather undetermined so far, is given basically by  $V_{\text{MU}}$  of [4] with small refinements stated below. The tensor-force component is exactly from  $V_{\text{MU}}$ , implying the  $\pi + \rho$  meson exchange force. It has been used in many cases [3, 4], and it has been accounted for microscopically under the new concept of Renormalization Persistency [25] where modern realistic effective interactions are analyzed in terms of the spin-tensor decomposition technique [26–28]. The central-force component of  $V_{\text{MU}}$  interaction has been determined in [4] so as to reproduce monopole properties of shell-model interactions SDPF-M ( $sd$ -shell part) and GXPF1A [22, 29] by a simple Gaussian interaction. We introduce here slight fine tuning with density dependence similar to the one in [27], in order that its monopole part becomes closer to that of GXPF1B. We include the two-body spin-orbit force of the M3Y interaction [30]. (For the present study, all these refinements produce minor changes, and do not change the overall conclusions. The refinements have been made so that the new Hamiltonian works well in a wide variety of nuclei other than those of this study.) Following USD and GXPF1B, all two-body matrix elements are scaled by  $A^{-0.3}$ . The single-particle energies (SPE) of  $sd$  shell are taken from USD, and those of  $pf$  shell are determined by requesting their effective SPEs on top of  $^{40}\text{Ca}$  closed shell equal to the single-particle energies of GXPF1B.

The Hamiltonian, referred to as SDPF-MU hereafter, is thus fixed prior to the shell model calculations presented in this paper. The diagonalization is performed by the MSHELL64 code [31]. The  $V_{\text{MU}}$  interaction has been used also to construct the cross-shell part of a recent shell-model Hamiltonian for  $p$ - $sd$  shell nuclei including neutron-rich exotic ones, providing with a good description of very light (B,C,N,O) nuclei [32].

We begin with the distribution of single-particle strength of proton  $sd$ -shell orbits. Spectroscopic factors obtained for  $^{48}\text{Ca}$  with the  $(e, e'p)$  reaction are displayed in the upper panels of Fig. 1 [9]. The  $0d_{5/2}$  single-particle strength is highly fragmented due to its high excitation energy (3-8 MeV range). The spectroscopic factors obtained by the present calculation are shown in the lower left-hand panel of Fig. 1, where an overall quenching factor 0.7 is used following the standard recipe to incorporate various effects of components outside the valence shell [33]. The agreement is excellent both in the position of peaks and their magnitudes. However, this agreement is lost, if the tensor force is removed from the cross-shell interaction, as shown in the right lower panel of Fig. 1. For instance, the largest  $0d_{3/2}$  and  $1s_{1/2}$  peaks are in the wrong order, and the strongest peaks of  $0d_{5/2}$  move towards higher energy. The  $0d_{3/2}$ - $0d_{5/2}$  gap of  $^{48}\text{Ca}$  turns out to be  $\sim 5$  MeV in the present calculation, but becomes  $\sim 2$  MeV larger, if the cross-shell tensor force is switched off.

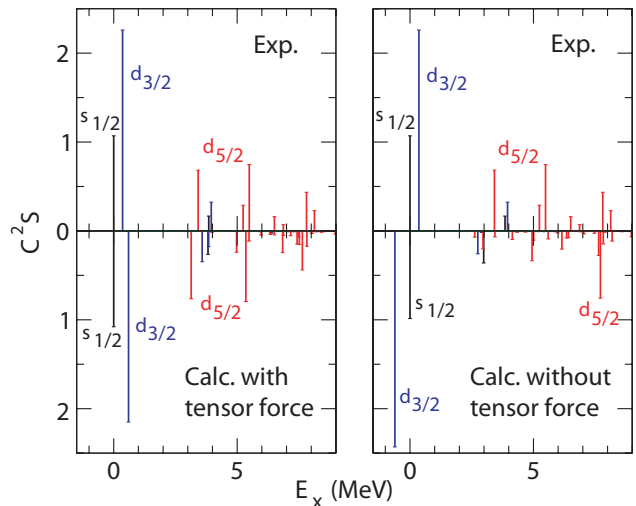


FIG. 1: (Color online) Spectroscopic factors of proton hole states measured by  $^{48}\text{Ca}(e,e'p)$  [9] (upper) and its theoretical calculation (lower left). The cross-shell tensor force is removed in lower right panel. The black, blue and red bars correspond to  $1s_{1/2}$ ,  $0d_{3/2}$  and  $0d_{5/2}$  states, respectively.

For  $^{40}\text{Ca}$ , although no experimental data by  $(e, e'p)$  reaction is available [34], Bastin *et al.* suggested a reduction of proton  $0d_{5/2}$ - $0d_{3/2}$  gap by 1.9 MeV from  $^{40}\text{Ca}$  to  $^{48}\text{Ca}$  based on reaction data [16]. Effective SPEs obtained from the SDPF-MU Hamiltonian are consistent with this and other experimental data [1]. On the other hand, the gap remains almost unchanged between  $^{40}\text{Ca}$  and  $^{48}\text{Ca}$ , if the cross-shell tensor force is removed. We note that the spectroscopic factor distributions for  $0d_{3/2}$  and  $1s_{1/2}$  were calculated also by a Green's function method by Barbieri [33], but there has been no previous report on the  $0d_{5/2}$  strength.

The proton shell structure thus evolves from  $^{40}\text{Ca}$  to  $^{48}\text{Ca}$ . Because only the tensor force can change the  $0d_{3/2}$ - $0d_{5/2}$  gap by this order of magnitude ( $\sim 2$  MeV), the agreement shown in Fig. 1 provides us with the first evidence from electron scattering experiments to the tensor-force-driven shell evolution induced by the mechanism of Otsuka *et al.* [3]. This agreement implies also the validity of the present SDPF-MU Hamiltonian, especially the interaction between the proton  $sd$  and neutron  $pf$  shells.

We now move to the shape transitions in exotic Si ( $Z=14$ ) and S ( $Z=16$ ) isotopes with even  $N=22-28$ . Before discussing quantitative results, we present an intuitive picture in Fig. 2 on the relation between the shell structure and the shape of Si nuclei. To begin with, we consider only two orbits  $0d_{5/2}$  and  $1s_{1/2}$  of protons for the sake of simplicity. In a conventional view,  $Z=14$  is a sub-magic number: no mixing between  $1s_{1/2}$  and  $0d_{5/2}$  due to large  $1s_{1/2}$ - $0d_{5/2}$  gap and/or weak mixing force. Six protons occupy all states of  $0d_{5/2}$  forming a closed subshell, as depicted in Fig. 2(a). This should end up

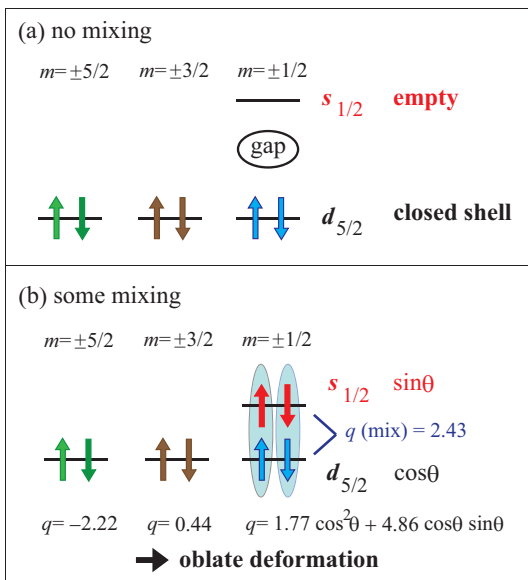


FIG. 2: (Color online) Intuitive illustration of the structure of intrinsic state at  $Z=14$ . Single-particle states of magnetic quantum numbers, denoted  $m$ , are shown.  $q$  implies intrinsic quadrupole moment ( $\text{fm}^2$ ) obtained with harmonic oscillator  $\hbar\omega=11.8$  MeV.

with a spherical shape for a doubly magic nucleus,  $^{42}\text{Si}$  ( $N=28$ ), similarly to  $^{34}\text{Si}$  ( $N=20$ ).

Figure 2 (b) indicates another situation where sizable mixing occurs between the  $1s_{1/2}$  and  $0d_{5/2}$  orbits in the case when the proton-neutron correlation is stronger than in Fig. 2 (a) and competes with  $1s_{1/2}$ - $0d_{5/2}$  spacing. The proton-neutron interaction, apart from its monopole part, can be modeled by a quadrupole-quadrupole interaction to a good extent. Effects of this interaction can be discussed in terms of intrinsic states due to a quadrupole deformation. Assuming an axially symmetric deformation, single-particle states of the same magnetic quantum numbers, denoted  $m$ , are mixed in the intrinsic states. Figure 2 (b) shows that this occurs for  $m = \pm 1/2$  between  $1s_{1/2}$  and  $0d_{5/2}$ , with amplitudes  $\sin\theta$  and  $\cos\theta$ , respectively. The phase of the mixing amplitude depends on the shape, prolate or oblate. In the case of Si isotopes, protons occupy the states of  $m = \pm 5/2, \pm 3/2$ , which yield in total a negative intrinsic quadrupole moment (oblate). The total intrinsic quadrupole moment gains a larger magnitude, if the  $1s_{1/2}$ - $0d_{5/2}$  mixing gives a negative moment. The contribution from the proton-neutron multipole interaction to the energy of total intrinsic state is proportional approximately to the product of the proton intrinsic quadrupole moment and the neutron one. Because a similar situation can occur for neutrons in  $1p_{3/2}$  and  $0f_{7/2}$  with a negative intrinsic moment produced mainly by the  $m = \pm 7/2$  component of  $0f_{7/2}$ , a stronger binding is obtained for the total intrinsic state

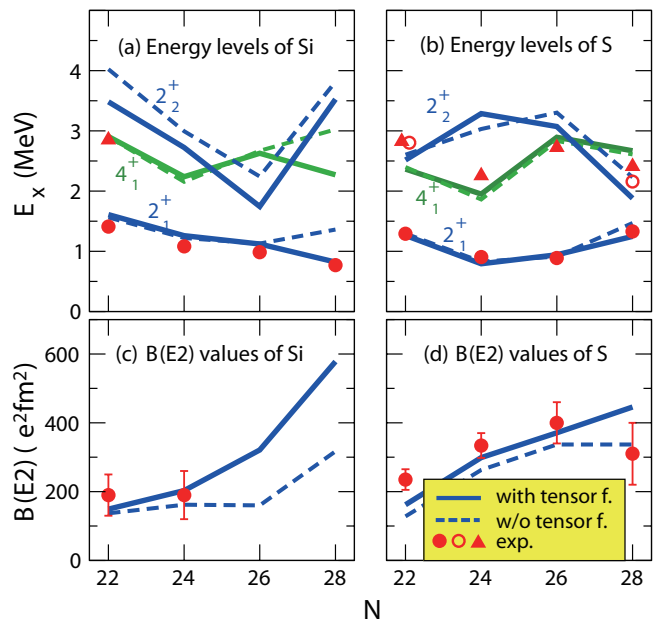


FIG. 3: (Color online) (a,b)  $2_{1,2}^+$  (blue lines and red circles) and  $4_1^+$  (green lines and red triangles) energy levels and (c,d)  $B(E2; 0_1^+ \rightarrow 2_1^+)$  values of Si and S isotopes for  $N=22-28$ . Symbols are experimental data [13–19]. Solid (dashed) lines are calculations with (without) the cross-shell tensor force.

with an oblate shape. Although the proton  $0d_{3/2}$  orbit is mixed to some extent in the actual shell-model calculation, the above mechanism still holds: the occupation of  $m = \pm 5/2$  remains with large negative quadrupole moment (oblate), and the mixing can occur among  $0d_{5/2}$ ,  $0d_{3/2}$  and  $1s_{1/2}$  orbits in the relevant  $m = \pm 1/2$  and  $\pm 3/2$  components in favor of the oblate shape.

This mechanism is of Jahn-Teller type, and it works if the mixing due to the proton-neutron correlation can compete with SPE spacings. The above intuitive pictures with Figs. 2 (a,b) suggest rather robustly that the shape of  $^{42}\text{Si}$  can be spherical or oblate, but not prolate. The  $0d_{5/2}$ - $1s_{1/2}$  spacing is 7.8 MeV for  $^{42}\text{Si}$  with the SDPF-MU Hamiltonian in the filling scheme. This is indeed comparable with the ground-state expectation value, -13.2 MeV, of multipole proton-neutron interaction, obtained by the shell-model calculation discussed below. Regarding the tensor force, when many neutrons occupy the  $0f_{7/2}$  orbital, the proton  $0d_{5/2}$  is raised due to the mechanism of Otsuka *et al.* [3] discussed for the ( $e, e'p$ ) data above. This effect is included in the result of SDPF-MU Hamiltonian, reducing  $0d_{5/2}$ - $1s_{1/2}$  spacing by 1.1 MeV for  $^{42}\text{Si}$ . We shall see its importance now.

We here investigate quantitatively the structure of Si and S isotopes in the context of the shell-model calculations with the SDPF-MU Hamiltonian. Figure 3 exhibits properties of even- $A$  Si and S isotopes. Effective charges are  $(e_p, e_n) = (1.35e, 0.35e)$  where an isoscalar shift fixed

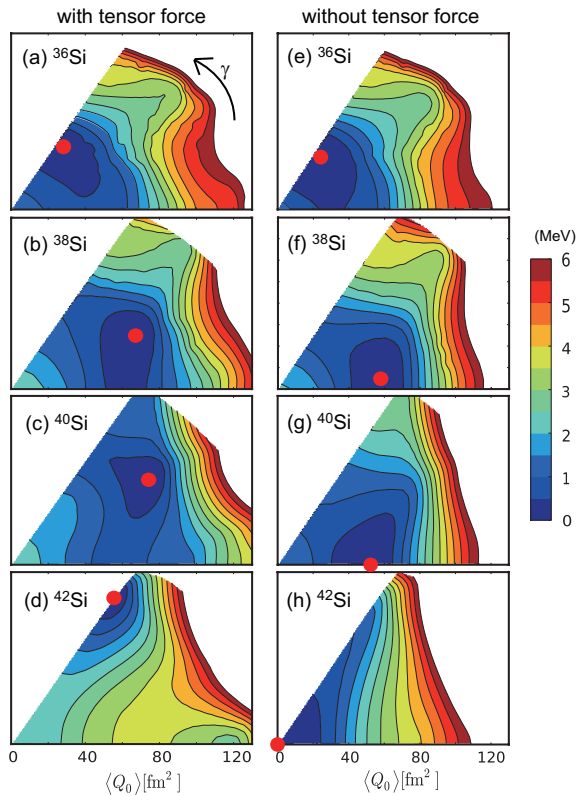


FIG. 4: (Color online) Potential energy surfaces of Si isotopes for  $\gamma=0\sim 60^\circ$  from  $N = 22$  to 28 calculated with (left) and without (right) the cross-shell tensor force. The energy minima are indicated by red circles.

for lighter isotopes are taken. The overall agreement with experiment is excellent in Fig. 3. For instance, in the present result,  $2_1^+$  levels of Si isotopes keep coming down as  $N$  increases consistently with experiment. The nice agreement suggests that the intuitive picture with Fig. 2 (b) works particularly well towards  $^{42}\text{Si}$ , resulting in a strongly deformed shape with low excitation energies consistent with recent measurement in GANIL [16]. However, if the tensor force is omitted from the cross-shell interaction, the  $2_1^+$  level of  $^{42}\text{Si}$  goes up, suggesting the case in Fig. 2 (a). Figure 3 exhibits results for S isotopes also in good overall agreement, including a bumpy behavior of the  $4_1^+$  level. Earlier shell-model calculations with empirical interactions [35, 36] give larger deviations and/or different trends from experiments. Different Hamiltonians are taken in [35] between  $Z \leq 14$  and  $Z \geq 15$  isotopes related to the monopole pairing strength in  $pf$  shell. The deviation from experiment becomes larger if this change is switched off. The present Hamiltonian is the same for all isotopes, and has been fixed prior to the shell-model calculations so as to make predictions.

The potential energy surface (PES) can be used to understand shapes contained in theoretical calculations. Figures 4 and 5 exhibit PES for Si and S isotopes, respec-

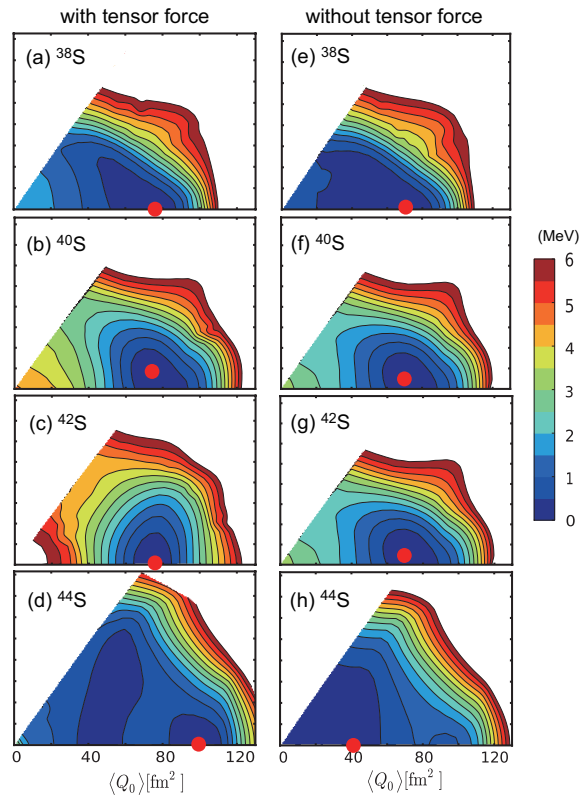


FIG. 5: (Color online) Potential energy surfaces of S isotopes from  $N = 22$  to 28. See the caption of Fig. 4.

tively, obtained by the constrained Hartree-Fock method [37] for the SDPF-MU Hamiltonian. The full Hamiltonian is taken in panels (a~d) of the two figures, whereas the cross-shell tensor force is removed in panels (e~h). We begin with PESs of Si isotopes (Fig. 4). Shape evolutions are seen clearly in both sequences (a~d) and (e~h), starting with similar patterns in  $^{36}\text{Si}$ . The shape evolves as more neutrons occupy  $pf$ -shell, with distinct differences between the two sequences. In (b,c), the deformation becomes stronger from (a) with triaxial minima, whereas the shape becomes more like modestly prolate in (f,g). In (d), one finds a strongly oblate shape with a sharp minimum, but the minimum is at the spherical shape in (h). This strong oblate deformation produces low  $2^+$  level and large  $B(E2)$  in Fig. 3 for the “doubly-closed”  $^{42}\text{Si}$ . Thus, the shape of exotic Si isotopes changes significantly within the range of  $\Delta N \sim 6$ . This feature is partly due to growing collectivity with more neutrons in the  $pf$  shell, but is also a manifestation of Jahn-Teller-type effect driven by the tensor force. Without the tensor force, the SPE spacings are too large, and the correlation energies cannot produce this effect.

The  $\gamma$ -unstable deformation is well developed in Fig. 4 (c), and this can be confirmed by the low-lying  $2_2^+$  level of  $^{40}\text{Si}$  in Fig. 3. This level seems to agree with a recent

$\gamma$ -ray experiment [15] where either of  $\gamma$ -rays 638(8) and 845(6) keV appears to feed directly the  $2_1^+$  state. We stress that the  $2_2^+$  level is sensitive to the tensor force through  $\gamma$ -instability in Si isotopes. In fact, the ratio  $E_x(2_2^+)/E_x(2_1^+)$  is as low as 1.5 for  $^{40}\text{Si}$ , whereas it becomes 4.4 for  $^{42}\text{Si}$ . The former is a prominent signature of  $\gamma$ -instability, while the latter is consistent with a vibration from a profound PES minimum of axially-symmetric deformation. Thus, the change from  $^{40}\text{Si}$  to  $^{42}\text{Si}$  is an intriguing example of the rapid and unexpected structure evolution. If the tensor force is switched off in the cross-shell interaction,  $E_x(2_1^+)$  of  $^{42}\text{Si}$  is raised but  $B(E2)$  value is still larger than that of  $^{40}\text{Si}$ . This is partly due to the stretched minimum in Fig. 4 (h) and partly due to relatively enhanced proton contribution in the E2 transition because of  $N=28$  closure.

The situation is quite different with PES of S isotopes (Fig. 5). With two more protons added to Si isotopes, the occupancy of the  $0d_{5/2}$  orbit is closer to that of a closed shell. The mixing between  $1s_{1/2}$  and  $0d_{3/2}$  then plays a decisive role, leading to a structure favoring prolate deformation. As for neutrons,  $m = \pm 7/2$  components of  $0f_{7/2}$  carry large negative intrinsic quadrupole moment and are crucial for oblate shape, while the others have positive or small negative values. In S isotopes, as protons favor prolate shapes, neutron sector becomes prolate for  $N < 28$ , by keeping the  $m = \pm 7/2$  states (almost) unoccupied. At  $N=28$ , the  $m = \pm 7/2$  states are occupied more. However, the neutron  $0f_{7/2}-1p_{3/2}$  spacing decreases from Ca isotopes to Si and S ones due to the vacancy of proton  $0d_{3/2}$ , and the excitation from the  $m = \pm 7/2$  states to other orbits does not cost much energy as compared to gains from proton-neutron correlation. This gives rise not to an oblate minimum but to triaxial softness. Thus, the shape is determined, in the present cases, primarily by the proton sector. We would like to emphasize the crucial role of protons in determining shapes of Si and S isotopes. We comment that the quasi SU(3) scheme [38], constructed for the configurations comprised of almost degenerate  $j$  and  $j - 2$  orbits only, *e.g.*,  $0f_{7/2}$  and  $1p_{3/2}$ , favors an oblate shape at  $N=28$ .

Panels (d) and (h) in Fig. 5 show prolate minima with opposite trends from panels (c,g) which are rather similar to each other. This difference arises within prolate shapes with shallow minima, and thereby its appearance in the energy levels is modest (See Fig. 3). The difference of the shapes between Si and S isotopes may suppress transfer reactions, for instance, two-proton removal from  $^{44}\text{S}$  [39].

We now discuss two-neutron separation energies ( $S_{2n}$ ) shown in Fig. 6. The agreement between experiment and the full calculation is quite good within  $\sim 0.5$  MeV, except for  $N=22$  Si value with discrepancy of 1.2 MeV due to the mixing of intruder configurations in  $^{34}\text{Si}$ , an issue outside this work. If the tensor force is switched off, deviations of 1-3 MeV occur for Si and S isotopes in the direction of larger  $S_{2n}$  values. This means that the tensor-force effect

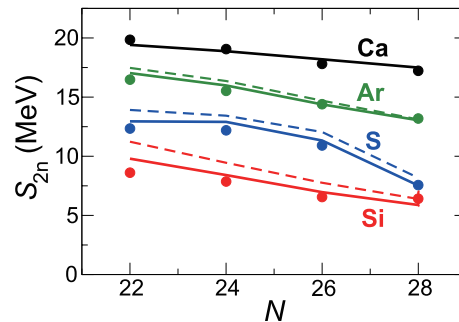


FIG. 6: (Color online) Two neutron separation energies of Si and S isotopes from  $N = 22$  to 28. Solid (dashed) lines are calculations with (without) the cross-shell tensor force. Points are experimental data [40, 41].

is repulsive and becomes larger from Ca to Si isotopes as a whole, consistently with the tensor-force-driven shell evolution. This evolution induces stronger deformation in some cases, *e.g.*,  $^{42}\text{Si}$ , where additional binding energy is gained and can cancel partly this repulsive effect.

While Si and S isotopes have been discussed with density-functional methods including appearance of oblate shapes [42–45], there are problems to be solved. No systematic calculations have been reported for levels and  $B(E2)$ 's of Si isotopes. The  $2_1^+$  level calculated in [45] reproduces experiment for  $^{44}\text{S}$ , but deviates by a factor of two for  $^{42}\text{Si}$ . Fig. 3 (a,b) shows that the  $2_1^+$  level of  $^{42}\text{Si}$  is sensitive to the tensor force, whereas that of  $^{44}\text{S}$  is not. The difference between  $^{42}\text{Si}$  and  $^{44}\text{S}$  in [45] might be relevant to this. The systematics of  $2_1^+$  level in S isotopes shows opposite trend in [44]. It will be also of interest to see single-particle properties given by these works. For instance, the proton  $0d_{5/2}-0d_{3/2}$  gap remains almost unchanged from  $^{40}\text{Ca}$  to  $^{48}\text{Ca}$  in these calculations, but this contradicts the trend seen in (e,e'p) data [9].

In summary, we have discussed the tensor-force driven reduction of the spin-orbit splitting by the mechanism of Otsuka *et al.* [3], for the first time, in terms of distribution of spectroscopic factors measured by  $^{48}\text{Ca}(e,e'p)$  experiment [9]. The SDPF-MU Hamiltonian has been introduced based on the  $V_{\text{MU}}$  interaction. The spectroscopic strength distribution provides a stringent test of this Hamiltonian. The levels,  $B(E2)$ 's and  $S_{2n}$  of exotic Si and S isotopes are described by the same Hamiltonian in a good agreement with all known experiments, exhibiting a rather rapid change, as a function of  $N$ , for Si isotopes but a quite different change for S isotopes. The tensor-force driven shell evolution [3] plays a crucial role in those shape transitions through the Jahn-Teller-type effect, including a robust mechanism that favors stable oblate shapes at sub-shell closures like  $^{42}\text{Si}$ . The  $B(E2)$  values are sensitive to the tensor force. The next region of the nuclear chart where such oblate shapes may occur is near  $^{78}\text{Ni}$ .

This work was in part supported by MEXT Grant-in-Aid for Scientific Research (A) 20244022 and for Young Scientists (B) (21740204) and NSF grant PHY-1068217. This work is a part of the CNS-RIKEN joint research project on large-scale nuclear-structure calculations.

- 
- [1] A. Gade and T. Glasmacher, *Prog. Part. Nucl. Phys.* **60**, 161 (2008); O. Sorlin and M.-G. Porquet, *Prog. Part. Nucl. Phys.* **61**, 602 (2008).
- [2] T. Otsuka *et al.*, *Phys. Rev. Lett.* **87**, 082502 (2001).
- [3] T. Otsuka *et al.*, *Phys. Rev. Lett.* **95**, 232502 (2005).
- [4] T. Otsuka *et al.*, *Phys. Rev. Lett.* **104**, 012501 (2010).
- [5] J. P. Schiffer *et al.*, *Phys. Rev. Lett.* **92**, 162501 (2004).
- [6] L. Gaudefroy *et al.*, *Phys. Rev. Lett.* **97**, 092501 (2006).
- [7] K. T. Flanagan *et al.*, *Phys. Rev. Lett.* **103**, 142501 (2009).
- [8] I. G. Darby *et al.*, *Phys. Rev. Lett.* **105**, 162502 (2010).
- [9] G. J. Kramer *et al.*, *Nucl. Phys. A* **679**, 267 (2001).
- [10] T. Otsuka *et al.*, *Nucl. Phys. A* **805**, 127c (2008).
- [11] H. A. Jahn and E. Teller, *Proc. Roy. Soc. A* **161**, 220 (1937).
- [12] P.-G. Reinhard and E. W. Otten, *Nucl. Phys. A* **420**, 173 (1984).
- [13] Evaluated Nuclear Structure Data File (ENSDF), <http://www.nndc.bnl.gov/ensdf/>.
- [14] X. Liang *et al.*, *Phys. Rev. C* **74**, 014311 (2006).
- [15] C. M. Campbell *et al.*, *Phys. Rev. Lett.* **97**, 112501 (2006).
- [16] B. Bastin *et al.*, *Phys. Rev. Lett.* **99**, 022503 (2002).
- [17] Z. M. Wang *et al.*, *Phys. Rev. C* **81**, 054305 (2010).
- [18] D. Sohler *et al.*, *Phys. Rev. C* **66**, 054302 (2007).
- [19] D. Santiago-Gonzalez *et al.*, *Phys. Rev. C* **83**, 061305(R) (2011).
- [20] B. A. Brown and B. H. Wildenthal, *Ann. Rev. Nucl. Part. Sci.* **38**, 29 (1988).
- [21] M. Honma *et al.* RIKEN Accel. Prog. Rep. **41**, 32 (2008).
- [22] M. Honma *et al.*, *Eur. Phys. J. A* **25**, s01, 499 (2005).
- [23] A. Poves and A. Zuker, *Phys. Rep.* **70**, 235 (1981).
- [24] Y. Utsuno *et al.*, *Phys. Rev. C* **60**, 054315 (1999).
- [25] N. Tsunoda *et al.*, *Phys. Rev. C* **84**, 044322 (2011).
- [26] M.W. Kirson, *Phys. Lett. B* **47**, 110 (1973).
- [27] B.A. Brown, W.A. Richter, R.E. Julies and B.H. Wildenthal, *Ann. Phys.* **182**, 191 (1988).
- [28] N. A. Smirnova *et al.*, *Phys. Lett. B* **686**, 109 (2010).
- [29] M. Honma *et al.*, *Phys. Rev. C* **69**, 034335 (2004).
- [30] G. Bertsch *et al.*, *Nucl. Phys. A* **284**, 399 (1977).
- [31] T. Mizusaki, N. Shimizu, Y. Utsuno, and M. Honma, code MSHELL64, unpublished.
- [32] C. Yuan, T. Suzuki, T. Otsuka, F. Xu and N. Tsunoda, *Phys. Rev. C* **85**, 064324 (2012).
- [33] C. Barbieri, *Phys. Rev. Lett.* **103**, 202502 (2009).
- [34] G. J. Kramer *et al.*, *Phys. Lett. B* **227**, 199 (1989).
- [35] F. Nowacki and A. Poves, *Phys. Rev. C* **79**, 014310 (2009).
- [36] K. Kaneko *et al.*, *Phys. Rev. C* **83**, 014320 (2011).
- [37] T. Mizusaki *et al.*, *Phys. Rev. C* **59**, R1846 (1999).
- [38] A.P. Zuker, *et al.*, *Phys. Rev. C* **52**, R1741 (1995).
- [39] J. Fridmann *et al.*, *Nature* **435**, 922 (2005).
- [40] G. Audi, A. H. Wapstra, and C. Thibault, *Nucl. Phys. A* **729**, 337 (2003).
- [41] B. Jurado *et al.*, *Phys. Lett. B* **649**, 43 (2007).
- [42] G.A. Lalazissis *et al.*, *Phys. Rev. C* **60**, 014310 (1999).
- [43] S. Peru *et al.*, *Eur. Phys. J. A* **9**, 35 (2000).
- [44] R. Rodriguez-Guzman *et al.*, *Phys. Rev. C* **65**, 024304 (2002).
- [45] Z. Li *et al.*, *Phys. Rev. C* **84**, 054304 (2011).